**Protein Purification and Reconstitution with Zn-protoporphyrin IX (ZnPP):** Apo $Fe_BMb1$ (without Fe(II) in the non-heme site) was purified according to known protocol.[1] Heme extraction was done using methylethylketone (MEK) followed by dialysis to remove MEK, using Teale's method[2]. Concentration of heme-extracted $Fe_BMb1$ was measured based on $\varepsilon_{280nm}$ = 30 $mM^{-1}cm^{-1}$. A stock solution of 8 mM Zn(II)-Protoporphyrin IX (ZnPP) (Frontier Scientific) was prepared in 66 mM NaOH. Care was taken so that the ZnPP stock solution and the protein during subsequent reconstitution process were not exposed to light. To 10 μM of heme-extracted $Fe_BMb1$ in 10 mM potassium phosphate pH 7, aliquots of ZnPP was added in 0.25 equivalents up to ~2.0 equivalents at 4°C with 30 minutes in between each addition. After the final addition of ZnPP, the solution was allowed to stir overnight to ensure that equilibrium was reached. The reconstituted protein was centrifuged (4°C, 30min, 11325rcf) to remove precipitate followed by concentration to ~5 mL. The bright magenta color protein was then passed down a small DEAE column pre-equilibrated in 50 mM Bis-Tris pH 7.3 to remove any excess ZnPP. This solution was then dialyzed in chelexed 50mM Bis-Tris pH 7.3 overnight to remove any adventitious metal ions. Final yield of the reconstituted protein was ~30%. Stock of $ZnPPFe_BMb1$ was stored at –80°C wrapped in foil. During subsequent handling of the protein for all the experiments, care was taken not to expose $ZnPPFe_BMb1$ to light. Incorporation of ZnPP into $Fe_BMb1$ was confirmed by UV-vis (Figure S1). Figure S1 shows that the spectral features of the reconstituted protein $ZnPPFe_BMb1$ (427 nm, 553 nm, 595 nm) are different from those of the cofactor ZnPP (386 nm, 554 nm, 588 nm) alone, suggesting that the cofactor was successfully incorporated into the protein.

**Determination of Extinction Coefficient of $ZnPPFe_BMb1$.** The extinction coefficient of $ZnPPFe_BMb1$ was determined using hemochromagen method,[3] with the exception that no dithionite was added. An extinction coefficient of $\varepsilon_{551nm}$ = 12.3 $mM^{-1}cm^{-1}$ for ZnPP-Pyridine complex[4] was used to determine the extinction coefficient of $ZnPPFe_BMb1$. Ratio of 0.066 M NaOH : Pyridine : $H_2O$ : Protein was 50: 33 : 13 : 4. A molar absorptivity of 136.2 $mM^{-1}cm^{-1}$ was determined using this modified hemochromagen method. Care was taken not to expose the protein to light during sample preparations, setting up crystal trays, and crystal soaking experiments

**Synthesis of $^{57}FeCl_2$.** $^{57}FeCl_2$ was synthesized inside the glove bag using the following procedure. 300 mL of DI $H_2O$ and 1 mL of 9.14% methanolic HCl (285.6 μL of 32% HCl + 714.4 μL methanol) was degassed and transferred into the glove bag. 25 mg $^{57}Fe$ metal (0.44 mmol) (Cambridge Isotope Lab) was taken in a small dry NMR tube and transferred into the glove bag. The degassed water was transferred into a small water bath and heated to ~60°C using a hot plate equipped with a stir bar. The NMR tube containing $^{57}Fe$ was immersed into the water bath and 350 μl of the 9.14% methanolic HCl (0.88 mmol) was added into the tube. $H_2$ evolution started immediately. The reaction was allowed to proceed for 3-4 hours until the gas evolution ceased. The solution was carefully transferred into a tared Schlenk flask with adaptor. The Schlenk flask was removed from the bag and immersed in dry ice/ethanol slush bath, and slowly opened to vacuum in a Schlenk line. The flask was then slowly warmed to 100°C using a water bath while in vacuum. After the solvent evaporated and the solid turned from green to white, the water bath was replaced with an oil bath and heated to 160°C, allowing the residual methanol to evaporate. The product was cooled to room temperature slowly, purged with Ar, sealed and weighed. The yield of $^{57}FeCl_2$ was ~65%.

**Fe(II) Titration.** UV-vis data were collected on a Cary 5000 spectrometer. For $FeCl_2$ titrations, aliquots of degassed metal stock solution were added using a gas tight syringe to a solution containing 1mL of 7μM $ZnPPFe_BMb1$ in 50 mM Bis-Tris pH 7.3 in an anaerobic cuvette (Starna cells). The protein was degassed in a Schlenk line and transferred to an anaerobic chamber (Coy laboratories) where the protein solution was prepared and transferred outside in the anaerobic cuvette for metal titration. Spectra were corrected for dilution and baseline. Difference spectra ($\Delta$Abs vs. $\lambda$) were obtained after subtracting the metallated spectra from the spectrum without Fe(II). Positive peaks were observed at 437 nm, 567 nm, 603 nm, while negative peaks are observed at 426 nm, 551 nm, 594 nm. Difference of difference absorbance ($\Delta\Delta$Abs) were obtained after subtracting the negative absorbance at 426 nm from positive absorbance at 437 nm during each Fe(II) addition and was plotted as a function of Fe(II) concentration (Figure S3 of the SI). This plot was analyzed by least square fits using[5]

$$y = y_{\max} * ([(P + x + k_D) - \{(P + x + k_D)^2 - (4 * P * x)\}^{\frac{1}{2}}]/2 * P)$$

Where, P = protein concentration in μM, and $K_d$ = dissociation constant. From this analysis, a dissociation constant of 7.2±0.4 μM was determined.

**EPR Spectroscopy.** EPR spectra were collected at liquid He temperatures on an X-band Varian E-122 spectrometer at the Illinois EPR Research Center equipped with an Air Products Helitran Cryostat, and EIP frequency counter. Calibration of magnetic fields was done using a Varian NMR Gaussmeter. Protein, buffers, and DEA NONOate ($\varepsilon_{250nm}$ = 9 $mM^{-1}cm^{-1}$) were degassed in a Schlenk line and transferred into the anaerobic chamber where the samples were prepared in 50 mM Bis-Tris pH 7.3. $FeCl_2$ stock solutions were prepared inside the glove bag by dissolving solid $FeCl_2$ in degassed water. For these preparations, the $Fe_B$ site was reconstituted with 1 eq. Fe(II), added in aliquots of 0.25 eq., followed by NO addition. Enough time was allowed to ensure metal binding, and NO evolution (~30 min). Each step was followed by checking the UV-vis spectra on an Agilent 8453 photodiode array spectrometer located inside the chamber. After NO addition, the protein was passed through a PD 10 column pre-equilibrated in

Bis-Tris pH 7.3 to remove impurities. Glycerol was added to a final concentration of 22%, then the solution was quickly flash frozen in liq. $N_2$ outside the glove bag. Spectra were fit using SIMPIPM.[6]

**EPR Power Saturation Experiments.** Efforts to characterize the radical-like species at $g \sim 2.01$ was undertaken. EPR power saturation experiments were performed with sample which was purified after NO addition using a small size exclusion column (same procedure as that of what is shown in Figure 5), at temperatures of 30K, 55K, 77K, and 111K with a varying microwave power from 0.03 to 31.6 or 50.2 mW (Figure S10). The peak to peak height of these spectra were measured and plotted as intensity/√power(mW) vs. microwave power (mW) (Figure S11). Analysis of the power saturation data at various temperatures was performed using the equation:[7]

$$I/\sqrt{P} = \frac{K}{\left[1 + \left(2^{\left(\frac{2}{B}\right)} - 1\right) * \left(\frac{P}{P_{1/2}}\right)\right]^{\frac{b}{2}}}$$

where I = peak-to peak intensity, $I_0$ = intensity at lowest power $P_0$, K = constant, P = microwave power in mW, b = measure of homogeneity of the line shape with a value varying between 1 and 3, $P_{1/2}$ is the microwave power at which the amplitude of the EPR signal is one-half of its unsaturated value.

These analyses gave $P_{1/2}$ values of 1.68±0.10, 8.73±1.01, 12.55±0.48, and 29.77±2.23 mW at 30K, 55K, 77K, and 111K, respectively (Table S1). These values of $P_{1/2}$ suggest that the radical is not a “free” radical, rather it is a most likely some sort of metal-associated radical.[7e, 8] We further simulated this signal under non-saturating conditions at 77K and 2 mW microwave power, see figure S12, and Table S2. Under non-saturating conditions the radical-like peak is present in ~5% relative population. From this simulation we obtained the $g_x$, $g_y$, and $g_z$ values of 2.013, 2.019, and 2.033, respectively, and with one nitrogen with a large hyperfine splitting of 78 MHz along the z direction and two other nitrogens with smaller nearly isotropic splittings partially resolved in the perpendicular feature. The *g* values indicate that this species is not a LS $\{FeNO\}^7$ complex based on what is known from literature.[9] In these LS iron complexes, one of the *g* values is greater than 2, another one is less than 2, and the third *g* values is in between the other two values, which is not the case in the our system. Thus, a definitive assignment of the identity of this radical-like species is not possible.

**ICP-MS.** ICP-MS analysis for Fe content on aliquots of the same EPR samples were performed at the University of Illinois microanalysis lab on a PerkinElmer – SCIEX ELAN DRCe instrument (Norwalk, CT USA).

**X-ray Crystallography.** Crystals were set up and grown at 4°C on hanging drops containing 0.1M sodium cacodylate pH 6.77, 0.2M NaOAC.3$H_2O$, 30-32% PEG 10K as well buffer. Drops contained an equal volume of 1.6 mM ZnPPFe$_B$Mb1 in 20 mM TRIS.$H_2SO_4$ pH 8 and the well buffer. ZnPPFe$_B$Mb1 crystals were frozen in a cryo protectant solution of 10 mM TRIS.$H_2SO_4$ pH 8, 50 mM cacodylate pH 6.8, and 30% PEG 400.

For $FeCl_2$ soaking, the crystals were transferred into an anaerobic chamber (Coy laboratories) in a cold room by multiple short cycles of vacuuming/purging. After transferring the tray into the anaerobic chamber, the cover slides were transferred to new wells containing freshly prepared degassed well buffers with some added solid dithionite and were left to equilibrate overnight to make them oxygen free. Selected crystals were then harvested, soaked in freshly degassed well buffer containing 0.1M MES pH 6.77, 0.2M NaOAC.3$H_2O$, 32% PEG 10K for 10 minutes, followed by soaking them in the same well buffer containing 10 mM $FeCl_2$ for 2 hrs. The crystals were then soaked in a cryo protectant solution of 10 mM TRIS.$H_2$SO4 pH 8, 50 mM MES pH 6.77, 30% PEG 400, and 10 mM $FeCl_2$, then flash frozen using liq. $N_2$ inside the glovebag.

Data were collected at the APS beamline 21-ID-D which supports tunable energy from 6.5-20 keV, equipped with MAR 300 CCD detector. The high resolution data were collected for 190 frames at 0.5s/frame, and a rotation of 0.5°/frame. Anomalous data were collected below and above Fe K-edge at 7.0, and 7.2 keV, respectively, for 380 frames at 0.3s/frame with a rotation of 0.5°/frame. Data were processed and scaled in HKL2000.[10] The structures were solved by molecular replacement using MolRep[11] in CCP4[12] suite of programs by using 3K9Z[1] as the search model after replacing the heme iron with Zn. The model was then refined in Refmac 5[13] and built in and completed in Coot[14] by using $2F_0 - F_c$ and $F_0 - F_c$ electron density maps. Anomalous electron density maps were generated in PHENIX,[15] and figures were made in PyMol[16] at a contour level of 7 sigma. ZnPPFe$_B$Mb1 and Fe(II)-ZnPPFe$_B$Mb1 were refined to 1.5 Å ($R_w$=20.7%, $R_f$=25.4%), and 1.52 Å ($R_w$=17.9%, $R_f$=21.9%) resolutions, respectively.

**Mössbauer Spectroscopy.** Mössbauer data were collected at Knox College, IL on an SEE Co. (Edina, MN) spectrometer, equipped with a constant acceleration transducer that uses a $^{57}$Co/Rh source. Initial radioactivity was 100 mCi. A Janis Super-varitemp cryostast, capable of recording temperatures from 4K to RT was used. Magnetic field strength was varied from 0.01-9T. Both low field and high field data were collected for the 4.2K spectra (Figures 6, S14) in the presence of 20 eq. NO. For higher temperatures 25K, 75K, 150K, data were collected only at low-field (0.01T) as shown in Figure S16 in the presence of 1 and 5 eq. NO. Data analysis was performed by custom built software using nonlinear least squares simultaneous fitting of multiple spectra to Spin Hamiltonian model (high field spectra) or fitting of a spectrum with Lorentzian lines (low-field spectra). For the data shown in Figure 6, all the S=3/2 species were simulated using slow relaxation model, while the S=2 species in 0.01T was simulated using fast relaxation model. For the data shown in Figure S14, the 0.01T data was simulated using fast relaxation model, while the high-field data were simulated using slow relaxation model. Samples were prepared using the same procedure as described in the EPR section, except freshly prepared $^{57}FeCl_2$ was used as the metal solution, and no glycerol was added. Samples were flash frozen in Mössbauer sample cups with inserts. The details of the high-field data obtained at 4.2 K in the presence of 20 eq. NO is described in the main text of the manuscript.

At low-field and 25K in the presence of 1 and 5 eq. NO, the S=3/2 $\{FeNO\}^7$ species is not observable due to intermediate relaxation of this species, leading to spectral broadening (Figure S16). At high temperatures, 75K and 150K, the $\{FeNO\}^7$ species is in the fast relaxation regime and can be detected and deconvoluted. The IS and QS values of the S=3/2 $\{FeNO\}^7$ obtained from these data (Table S4) are close to the values obtained from the high field data measured at 4.2 K containing 20 eq. of NO (see Tables 2 and S3). At higher temperatures all of the S=3/2 species is close to the fast relaxation limit for which the magnetic hyperfine splitting collapses to a single doublet (Figure S16, green line), unlike at low temperature where a magnetically split component is also observed (Figure 6: gray short dotted line, Figure S15: green line). The position of the S=3/2 doublet shown in green (Figure S16) is similar to the S=3/2 species present in intermediate relaxation at 4.2K with 20 eq. NO (Figure 6: gray dashed line, Figure S15: gray solid line), indicating that the same S=3/2 species is formed irrespective of temperature and NO equivalents. While the exact cause for a fraction of the S=3/2 species to be in intermediate relaxation at low temperature (Figure 6: gray dashed line, Figure S15: gray solid line) is uncertain, it seems plausible that the presence of this center in close proximity to other paramagnetic centers e.g. the radical-like species observed in EPR would make these centers to be in intermediate relaxation regime due to spin-spin relaxation processes.

## Computational Details:

### System Preparation and Equilibration Procedure.

Two sets of independent calculations were performed: the first set was without NO and the second set was with NO bound. The system preparation and solvent equilibration were performed with DESMOND.[17] The initial protein geometry for the first set of calculations was obtained from the crystal structure shown in Figure 3. Hydrogens were added to the heavy atoms using DESMOND. This structure was immersed in an orthorhombic box of TIP3P water molecules, in which the distance between the molecule and the boundary was at least 10 Å, and the overall charge of the system was neutralized by the addition of three $Cl^-$ ions. For the second set of calculations, the optimized geometry from the QM/MM calculation of the protein without NO was taken as the initial protein structure with NO added at the Fe center. The AMBER-03[18] force field parameters were used during the solvent equilibration. The parameters for Zn-protoporphyrin (ZnPP) were chosen to be the same as those for heme,[19] where the Fe center has been replaced by Zn. For NO, the bond length was determined from a separate DFT calculation with the B3LYP functional,[20] and 6-31G** basis set,[21] and the ChelpG charges were used to represent the partial charges. All of the heavy-atom hydrogen bonds were constrained using the SHAKE algorithm as implemented in DESMOND. The solvent equilibration procedure utilized to obtain the starting configurations for the subsequent QM/MM calculations was as follows:

1) Energy of the solvent (water molecules and $Cl^-$ ions) was minimized with a restraining potential of 100 kcal/mol on the solute (protein + ZnPP and NO, when present);
2) 100 ps of solvent equilibration was performed under constant NPT condition at 298 K and 1.01325 atm, maintaining the restraining potential on the solute;
3) 1 ns of solvent equilibration was performed under constant NVT conditions at 298 K, maintaining the restraining potential on the solute.

## Details of QM/MM Calculations.

The QM/MM calculations were performed with the Q-Site package,[22] which uses Jaguar for the QM part of the calculations and IMPACT for the MM portion. The QM part of the system was described by DFT with the B3P86 functional,[20a, 20e, 23] and LACVP** (6-31G** for non-metals and lanl2dz for the Fe and Zn centers) basis set.[21] The QM region included the Glu68, His29, His43, His64, and His93 residues along with the Fe-center, ZnPP, and NO. The histidine residues were H-capped at the C4-C$\beta$ position, while C$\alpha$-C$\beta$ was H-capped for the glutamate residue to provide flexibility to the coordination mode of the –COO group. All of the substituents of the porphyrin ring were H-capped. The MM part of the system was described by the OPLS2005 force field.[24] All atoms outside a sphere with a 20 Å radius centered at the Fe remained fixed during the QM/MM calculations. The QM-MM interface was modeled by the frozen localized molecular orbital method that is implemented in Q-Site. The spin multiplicities of the QM region for the calculations without and with NO were 5 and 4, respectively, while the molecular charge was +1 in both cases. The structures of the QM region without and with NO are shown in Figure S17. As discussed in the main paper, the electronic description of the NO bound structure corresponds to [$Fe^{2+}$-$NO^{\bullet}$]. Separate attempts to converge to a geometry with the electronic configuration similar to [$Fe^{3+}$-$NO^{-}$] converged to [$Fe^{2+}$-$NO^{\bullet}$].

### Calculations of Mössbauer properties

DFT calculations have been successfully used in investigating Mössbauer properties of non-heme Fe proteins such as soybean monoxygenases,[25] isopenicillin N-synthase (IPNS),[26] hydroxylase,[27] and ferric uptake regulation protein.[28] Previous studies combining quantum chemical and Mössbauer spectroscopic investigations have also enabled structure refinement and determination of iron sites in a number of iron protein systems,[26, 28-29] including specifically an S=3/2 $\{FeNO\}^7$ protein complex IPNS·ACV·NO (ACS is the substrate of IPNS) as well as model complexes.[26, 30] Here, such investigations are also applied to calculate the Mössbauer parameters of Fe(II)-ZnPPFe$_B$Mb1 in the absence and presence of NO.

The $^{57}$Fe quadrupole splitting ($\Delta E_Q$) arises from the non-spherical nuclear charge distribution in the I*=3/2 excited state in the presence of an electric field gradient at the $^{57}$Fe nucleus, while the isomer shift ($\delta_{Fe}$) arises from differences in the electron density at the nucleus between the absorber (the molecule or system of interest) and a reference compound (usually $\alpha$-Fe at 300K). The former effect is related to the components of the electric field gradient (EFG) tensor at the nucleus as follows:[31]

$$\Delta E_Q = \frac{1}{2} eQV_{zz}\left(1+\frac{\eta^2}{3}\right)^{1/2} \tag{1}$$

where $e$ is the electron charge, $Q$ is the quadrupole moment of the E*=14.4 keV excited state, and the principal components of the EFG tensor are labeled according to the convention:

$$|V_{zz}| > |V_{yy}| > |V_{xx}| \tag{2}$$

with the asymmetry parameter being given by:

$$\eta = \frac{V_{xx}-V_{yy}}{V_{zz}} \tag{3}$$

The isomer shift in $^{57}$Fe Mössbauer spectroscopy is given by:[32]

$$\delta_{Fe} = E_A - E_{Fe} = \frac{2\pi}{3} Ze^2\left(< R^2 >^* - < R^2 >\right)\left(|\psi(0)|^2_A - |\psi(0)|^2_{Fe}\right) \tag{4}$$

where Z represents the atomic number of the nucleus of interest (iron) and R, R* are average nuclear radii of the ground and excited states of $^{57}$Fe. Since $|\psi(0)|^2_{Fe}$ is a constant, the isomer shift (from Fe) can be written as:

$$\delta_{Fe} = \alpha\,[\,\rho(0) - c\,] \tag{5}$$

where $\alpha$ is the so-called calibration constant and $\rho(0)$ is the computed charge density at the iron nucleus. Both $\alpha$ and c can be obtained from the correlation between experimental $\delta_{Fe}$ values and the corresponding computed $\rho(0)$ data in a training set. Then, one can use equation (5) to predict $\delta_{Fe}$ for a new molecule from its computed $\rho(0)$, basically as described in detail elsewhere for a wide variety of heme and other model systems.[32] The hybrid functional B3LYP[33] with a Wachter's basis for Fe,[34] 6-311G* for all the other heavy atoms and 6-31G* for hydrogens was used to predict Mössbauer quadrupole splittings and isomer shifts, the same approach used in the previous work for various iron-containing proteins and models with experiment-versus-theory linear correlation coefficients $R^2$=0.98 and 0.97, respectively.[26, 28-32, 35] These systems cover a broad range of iron systems, including all iron spin states and all coordination states. In particular, this method was found to well reproduce the Mössbauer quadrupole splittings and isomer shifts in an S=3/2 $\{FeNO\}^7$ protein complex IPNS·ACV·NO (ACS is the substrate of IPNS) as well as model complexes.[26, 30] To calculate $\Delta E_Q$, we first evaluated the principal components of the electric field gradient tensor at the $^{57}$Fe nucleus ($V_{ii}$), then we used equation (1) to deduce $\Delta E_Q$, using a precise recent determination of Q = 0.16 (±5%) x $10^{-28}$m$^2$,[36] a value previously found to permit excellent accord between theory and experiment in a broad range of systems.[26, 28-32, 35] To calculate $\delta_{Fe}$ values, we read the Kohn-Sham orbitals from the *Gaussian 09*[37] results into the AIM 2000 program,[38] to evaluate the charge density at the iron nucleus, $\rho(0)$. Then, we evaluated the isomer shifts by using the equation derived previously:[32]

$$\delta_{Fe} = -0.404\ [\rho(0) - 11614.16] \qquad (6)$$

All the quantum chemical calculations were performed using *Gaussian 09*. [37]

As there is no X-ray structure of the NO-bound form of Fe(II)-ZnPPFe$_B$Mb1 protein, we used geometry optimized model to investigate its Mössbauer properties. To account for the protein environment effect to a reasonable extent within the limit of quantum chemical computing resources, based on the previous investigation of various levels of truncations for quantum chemical models,[39] we kept all the ligands around iron, water plus the iron bound amino acid ligands (E68, H29, H43, H64), with these protein residues modeled up to the backbone C$\alpha$ positions which are fixed at the X-ray crystal structure positions of the NO-free protein. All other atomic positions were allowed to be optimized. It is interesting to note that the NO-free Fe(II)-ZnPPFe$_B$Mb1 non-heme site contains a vacant binding site similar to the five-coordinate active site of IPNS bound with its substrate ACV, [26] and the experimental Mössbauer properties of the NO-bound form (see Table 2) are also similar to the experimental Mössbauer properties of S=3/2 six-coordinate NO-bound protein complex IPNS·ACV·NO ($\delta_{Fe}$: 0.65 mm/s; $\Delta E_Q$: 1.20 mm/s), as well as a small model complex $Fe(L)(NO)(N_3)_2$ (L=*N*,*N'*,*N*"-trimethyl-1,4,7-triazacyclononane; $\delta_{Fe}$: 0.62 mm/s; $\Delta E_Q$: –1.28 mm/s) with an X-ray structure.[26] Therefore, NO was inserted in the vacant site of the NO-free Fe(II)-ZnPPFe$_B$Mb1 non-heme site in the initial structure for subsequent geometry optimization, using the BPW91 method[40] with the same basis described above, which was used previously in structural investigations for a number of iron proteins.[28, 29b, 41] A number of initial NO orientations were chosen based on the available spaces in this site, which all converged to the same optimized structure as shown in Figure S18, in which NO's oxygen has a weak hydrogen bonding interaction with water's hydrogen (2.545 Å) while the original strong hydrogen bond between water's other hydrogen atom and E68 is maintained. As shown in Table 2, both Mössbauer quadrupole splittings and isomer shifts in the S=2 NO-free non-heme site and the S=3/2 NO-bound protein complexes are in good agreement with experimental data. In this optimized structure (Figure S18), the Fe-NO bond length is 1.768 Å, which is similar to the 1.738 Å value of the Fe-NO bond length in the X-ray structure of a S=3/2 $\{FeNO\}^7$ small model compound $Fe(L)(NO)(N_3)_2$. The slightly longer bond length in this protein model versus the small model complex is consistent with their experimental isomer shifts, since in the protein case, the longer bond length is usually associated with decreased ligand charge contribution to the iron center, and the relatively smaller charge density at the iron nucleus then leads to a relatively larger isomer shift based on equation (6), as observed experimentally (0.69 mm/s vs. 0.62 mm/s). The Mulliken spin population analysis shows that in this NO-bound non-heme site, iron has 3.79 unpaired electrons and the NO moiety has −1.09 unpaired electrons, which is essentially the Fe(S=2) center anti-ferromagnetically coupled with NO (S=1/2). This is again in good accord of previous work of similar S=3/2 $\{FeNO\}^7$ protein and models with excellent Mössbauer property predictions. [26, 30] It is also consistent with the QM/MM results as described in the text. Previous work show that although other types of electronic configurations other than the Fe(S=2) coupled with NO(S=−1/2) may be obtained by using other theoretical methods, the predicted Mössbauer properties from using other electronic configurations are worse than the currently used method and electronic configuration. [26, 30] These results show that the NO bound structure determined from this quantum chemical investigation is consistent with the experimentally measured Mössbauer properties for this NOR biosynthetic model, and also consistent with previously obtained six-coordinate S=3/2 $\{FeNO\}^7$ protein and models.[26]

**Table S1.** Parameters extracted from fits of the EPR power saturation data shown in Figures S10, and S11.

| **T(K)** | **K** | **b** | **$P_{1/2}$ (mW)** |
|---|---|---|---|
| 30 K | 124±2 | 1.23±0.02 | 1.68±0.10 |
| 55 K | 75±3 | 1.25±0.10 | 8.73±1.01 |
| 77 K | 66±1 | 1.27±0.03 | 12.55±0.48 |
| 111 K | 44±2 | 2.0±0.6 | 29.77±2.23 |

**Table S2.** EPR parameters extracted from simulation of the spectrum shown in Figure S12.

| $g_x$ | $g_y$ | $g_z$ | $A_x$ (MHz) | $A_y$ (MHz) | $A_z$ (MHz) |
|---|---|---|---|---|---|
| 2.013 | 2.019 | 2.033 | 12.51 | 10.95 | 78.17 |
| | | | 18.64 | 11.58 | 17.39 |
| | | | 18.47 | 12.54 | 16.79 |

**Table S3.** Full Mössbauer parameters for $^{57}$Fe(II)-Fe$_B$Mb1 (Figure S14), and $^{57}$Fe(II)-Fe$_B$Mb1 in the presence of 20 eq. NO (Figure 6). ~65% of the S=3/2 {FeNO}$^7$ complex is formed at the Fe$_B$ site in the presence of NO, with 35% of $^{57}$Fe(II) remaining unreacted as S=2 HS ferrous. Eta values obtained from DFT calculation of partially optimized active site structure are shown as bold in parenthesis.

| **Sample** | **$\delta_{Fe}$ (mm/s)** | **$\Delta E_Q$ (mm/s)** | **%** | **$\Gamma$ (mm/s)** | **$\eta$** | **D ($cm^{-1}$)** | **E ($cm^{-1}$)** | **E/D** | **A/(g*beta) (T)** | **Euler angles (D→Q) (°)** | **S** |
|---|---|---|---|---|---|---|---|---|---|---|---|
| $^{57}$Fe-ZnPPFe$_B$Mb1 | 1.13±0.01 | 2.85±0.01 | 100 | 0.35 | 0.26<br>(**0.26**) | 2.3 | 0.43 | 0.19 | −2.7, −9.3, −24.1 | 86, −83, −85 | 2 |
| $^{57}$Fe-ZnPPFe$_B$Mb1-NO | 0.69±0.01 | −1.70±0.01 | 65 | 0.30 | 0.30<br>(**0.85**) | 7.2 | 0.79 | 0.11 | −22.5, −21.0, −35.1 | 43, 19, 0 | 3/2 |

**Table S4.** Mössbauer parameters extracted from fits of the data shown in Figure S16. The parameters for the S=2 Fe(II) starting material is shown in black, while those of the S=3/2 {FeNO}$^7$ complex are shown in red. [a]The sign of QS cannot be determined at low field because in the absence of an applied field, a non-Kramers system like a high-spin ferrous iron center usually have no magnetic splitting in its spectrum. In a large applied field, one can distinguish the sign of the quadrupole splitting through asymmetry of the magnetic splitting between the higher- and lower-velocity lines of a quadrupole doublet. Thus, in the absence of magnetic splitting it is impossible to determine the sign of the quadrupole splitting. [b]Due to intermediate relaxation, leading to very broad spectral widths, the parameters for the S=3/2 {FeNO}$^7$ species could not be obtained from the fits of the 25K data. [c]For a paramagnetic center with an intermediate spin relaxation rate, the magnetic structure of its Mössbauer spectrum will have nearly collapsed, leaving a much-broadened quadrupole doublet. It is usual for one line of the quadrupole doublet in this situation to have a narrower linewidth than the other line. Therefore, in a good fit to the S=3/2 quadrupole lines, the two lines have unequal linewidth

| **Sample** | **T (K)** | **$\delta_{Fe}$ for S=2 Fe(II) species (mm/s)** | **$\Delta E_Q$ for S=2 Fe(II) species (mm/s)** | **$\Gamma$ for S=2 Fe(II) species (mm/s)** | **$\delta_{Fe}$ for S=3/2 {FeNO}$^7$ species (mm/s)** | **$\Delta E_Q$ for S=3/2 {FeNO}$^7$ species (mm/s)** | **$\Gamma$ for S=3/2 {FeNO}$^7$ species (mm/s)** |
|---|---|---|---|---|---|---|---|
| **$^{57}$Fe-ZnPPFe$_B$Mb1+ 1eq. NO** | 25 | 1.15 | 2.84$^a$ | 0.38 | ND$^b$ | ND$^b$ | ND$^b$ |
| | 75 | 1.13 | 2.84$^a$ | 0.36 | 0.87 | 1.44$^a$ | 0.98,$^c$ 0.67$^c$ |
| | 150 | 1.09 | 2.83$^a$ | 0.32 | 0.78 | 1.66$^a$ | 0.70 |
| **$^{57}$Fe-ZnPPFe$_B$Mb1+ 5eq. NO** | 25 | 1.14 | 2.83$^a$ | 0.43 | ND$^b$ | ND$^b$ | ND$^b$ |
| | 75 | 1.12 | 2.84$^a$ | 0.39 | 0.89 | 1.15$^a$ | 0.95,$^c$ 0.64$^c$ |
| | 150 | 1.11 | 2.82$^a$ | 0.33 | 0.78 | 1.61$^a$ | 0.96$^c$, 0.60$^c$ |

**Table S5.** Data collection and refinement statistics of ZnPPFe$_B$Mb1.

| **Data Collection Statistics** | |
|---|---|
| Data Set | Native |
| Space Group | P 21 21 21 |
| Unit Cell | a = 39.754, b = 48.233, c = 77.819<br>$\alpha = 90, \beta = 90, \gamma = 90$ |
| Wavelength (Å) | 1.0781 |
| Resolution (Å)[1] | 50.00-1.50 (1.53-1.50) |
| $R_{sym}$ (%)[2] | 4.4 (64.3) |
| $<I/\sigma I>$[3] | 10 (2) |
| Completeness (%)[4] | 98.9 (87.7) |
| Redundancy | 4.9 (4.5) |
| Beamline | LS-CAT-21-ID-D |
| **Refinement Statistics** | |
| Resolution (Å) | 1.50 (30.28-1.50) |
| R-Factor (%)[10] | 20.7 |
| $R_{free}$ (%)[11] | 25.5 |
| Protein atoms[12] | 1268 |
| Water Molecules | 185 |
| Unique Reflections | 23195 |
| R.m.s.d.[13] | |
| Bonds (Å) | 0.021 |
| Angles (˚) | 2.669 |

**Table S6.** Data collection and refinement statistics of Fe(II)-ZnPP$\mathrm{Fe_B}$Mb1.

| **Data Collection Statistics** | |
|---|---|
| Data Set | Native |
| Space Group | P 21 21 21 |
| Unit Cell | a = 39.750, b = 39.750, c = 76.008<br>$\alpha = 90, \beta = 90, \gamma = 90$ |
| Wavelength (Å) | 1.0781 |
| Resolution (Å)$^1$ | 50.00-1.52 (1.55-1.52) |
| $R_{sym}$ (%)$^2$ | 3.2 (58.5) |
| $<I/\sigma I>^3$ | 10 (1) |
| Completeness (%)$^4$ | 98.7 (98.2) |
| Redundancy | 3.7 (3.6) |
| Beamline | LS-CAT-21-ID-D |
| **Refinement Statistics** | |
| Resolution (Å) | 1.52 (40.34-1.52) |
| R-Factor (%)$^{10}$ | 17.9 |
| $R_{free}$ (%)$^{11}$ | 21.9 |
| Protein atoms$^{12}$ | 1244 |
| Water Molecules | 149 |
| Unique Reflections | 19965 |
| R.m.s.d.$^{13}$ | |
| Bonds (Å) | 0.021 |
| Angles (˚) | 2.755 |

**Table S7.**

| **Data Collection Statistics** | | |
|---|---|---|
| Data Set | Anomalous_below Fe Edge | Anomalous_above Fe Edge |
| Space Group | P 21 21 21 | P 21 21 21 |
| Unit Cell | a = 39.66, b = 47.55, c = 75.93<br>$\alpha = 90, \beta = 90, \gamma = 90$ | a = 39.65, b = 47.56, c = 75.96<br>$\alpha = 90, \beta = 90, \gamma = 90$ |
| Wavelength (Å) | 1.7713 | 1.7220 |
| Resolution (Å)[1] | 50.00-1.85 (1.88-1.85) | 50.00-1.81 (1.84-1.81) |
| $R_{sym}$ (%)[2] | 6.1 (58.9) | 6.4 (65.0) |
| $<I/\sigma I>$[3] | 20 (2) | 10 (1) |
| Completeness (%)[4] | 99.9 (98.2) | 99.9 (99.9) |
| Redundancy | 7.0 (4.9) | 6.9 (4.8) |
| Beamline | LS-CAT-21-ID-D | LS-CAT-21-ID-D |

[1] Statistics for highest resolution bin of reflections in parentheses.

[2] $R_{sym} = \Sigma_h \Sigma_j | I_{hj} - <I_h> | / \Sigma_h \Sigma_j I_{hj}$, where $I_{hj}$ is the intensity of observation j of reflection h and $<I_h>$ is the mean intensity for multiply recorded reflections.

[3] Intensity signal-to-noise ratio.

[4] Completeness of the unique diffraction data.

[5] Resolution cut-off used during heavy-atom refinement and phase calculations.

[6] $R_{iso} = \Sigma | |F_{ph}| - |F_p| | / \Sigma |F_p|$, where $F_p$ and $F_{ph}$ are the native and heavy-atom structure factor amplitudes, respectively.

[9] Number of heavy-atom sites per asymmetric unit.

[10] R-factor = $\Sigma_h | |F_o| - |F_c| | / \Sigma_h |F_o|$, where $F_o$ and $F_c$ are the observed and calculated structure factor amplitudes for reflection h.

[11] $R_{free}$ is calculated against a 10% random sampling of the reflections that were removed before structure refinement. [12] Total number of protein atoms refined in the asymmetric unit.

[13] Root mean square deviation of bond lengths and bond angles.

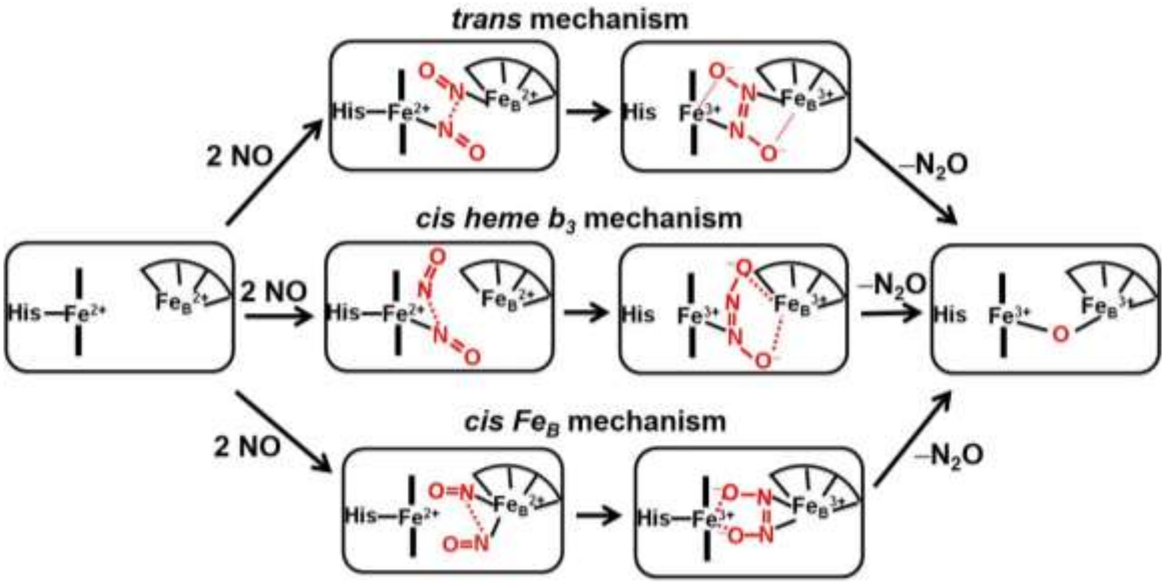

**Scheme S1.** Schematic representation of the *trans, cis* heme $b_3$, and *cis* Fe$_B$ mechanisms. In the proposed *cis*-heme $b_3$ mechanism, after one NO is bound to the heme $b_3$ site, a free NO electrophilically attacks this heme bound NO. In the *cis* Fe$_B$ mechanism, two molecules of NO bind to the Fe$_B$ site, whereas the *trans* mechanism suggests one NO binds to heme $b_3$ and the Fe$_B$ site simultaneously for the N-N bond formation to occur.

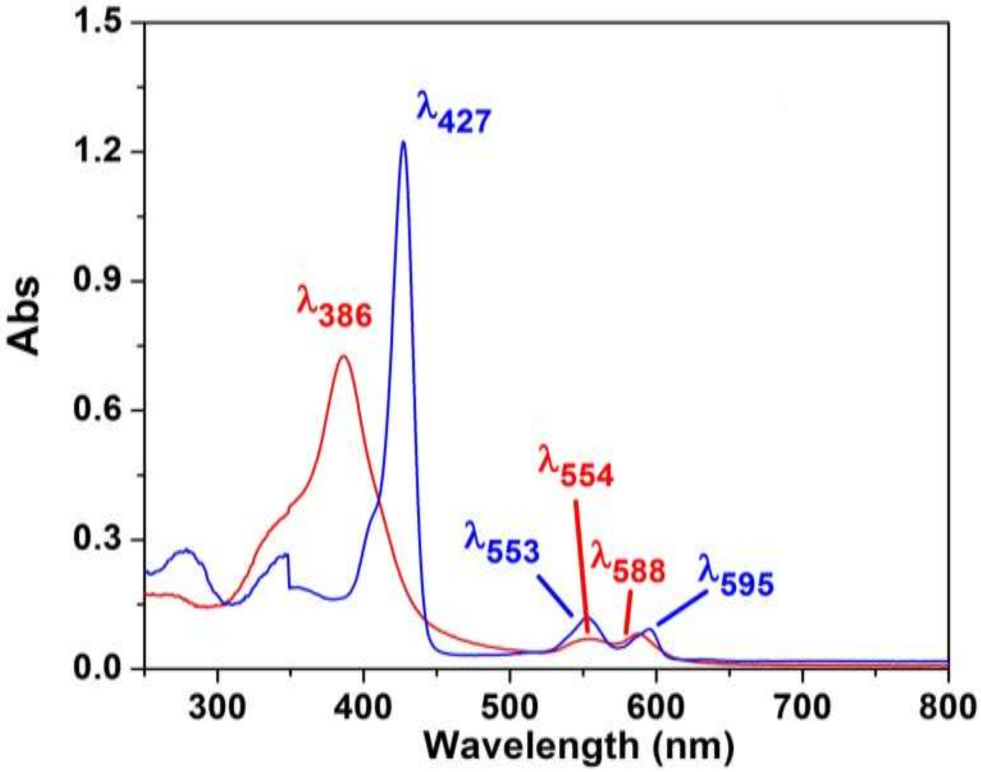

**Figure S1.** UV-vis spectra of ZnPP (red) and ZnPPFe$_B$Mb1 in 100 mM potassium phosphate pH 7 (blue), recorded on a Cary 5000 spectrophotometer. The spectral features of the reconstituted protein ZnPPFe$_B$Mb1 (427 nm, 553 nm, 595 nm) are different from those of the cofactor ZnPP (386 nm, 554 nm, 588 nm) alone, confirming that the cofactor is incorporated into the protein.

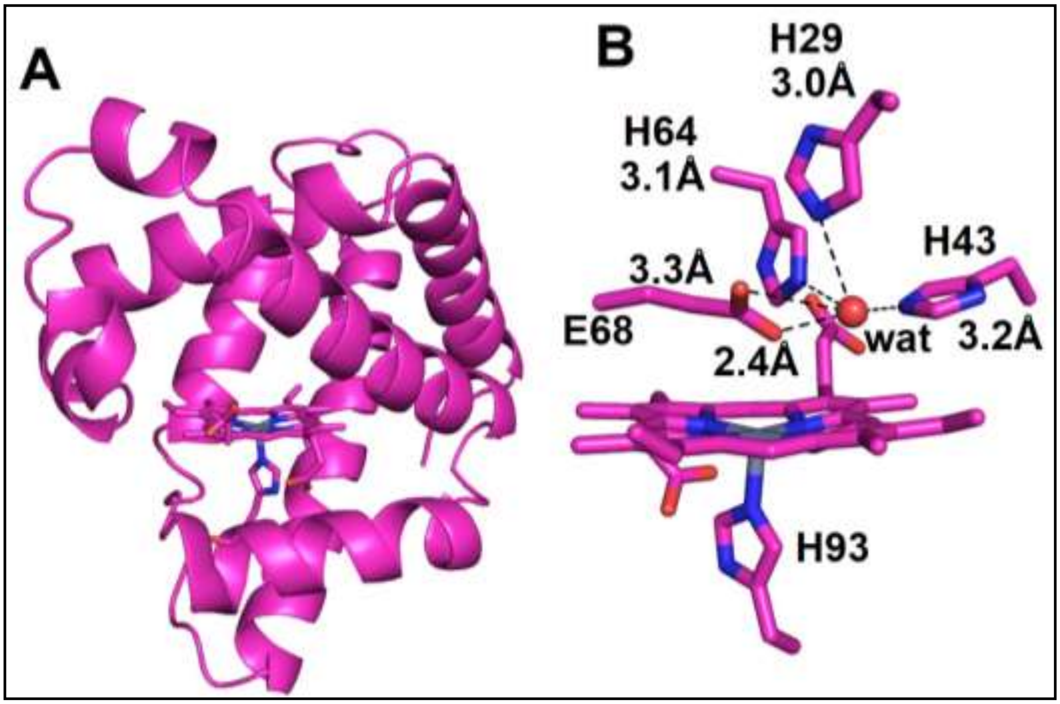

**Figure S2.** X-ray structure of apo $ZnPPFe_BMb1$ refined to 1.5 Å. A) Cartoon representation of the protein is shown. ZnPP and His93 are shown as sticks. B) Residues in the distal pocket are shown as sticks. The water molecule is shown as a red sphere. Distances from the water molecule to the nearby residues in the pocket are also shown. $R_w$ = 20.7%, $R_f$ = 25.4%. Coordinates and structure factors have been deposited with the PDB code 4MXL.

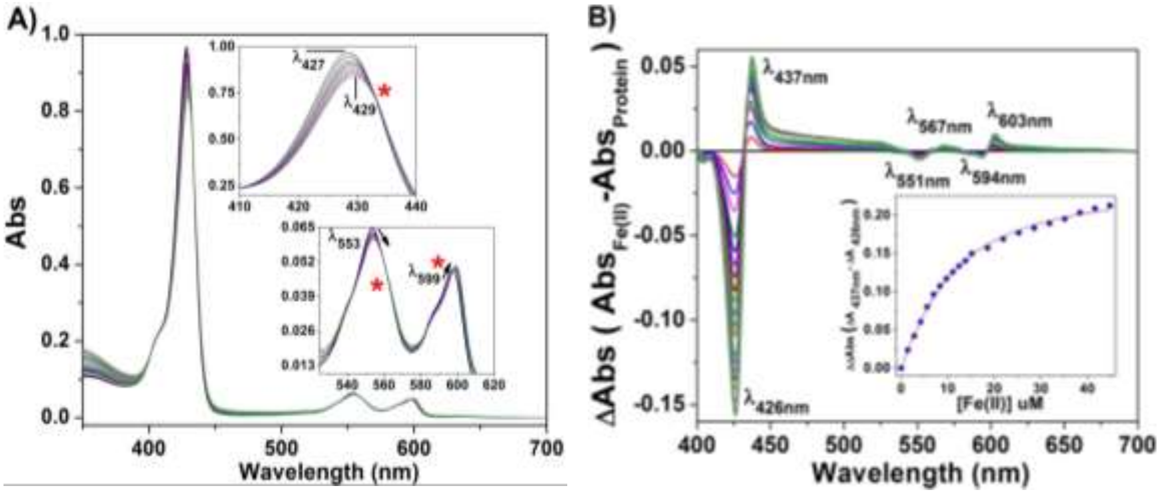

**Figure S3. A)** UV-vis spectra obtained during titration of aliquots of $FeCl_2$ to 7 μM $ZnPPFe_BMb1$ in 50 mM Bis-Tris pH 7.3. Insets show blow-ups of the Soret and visible regions. Isosbestic points are shown as asterisk. **B)** Difference spectra (ΔAbs vs. λ) were obtained after subtracting the metallated spectra from the spectrum without Fe(II). Positive peaks were observed at 437 nm, 567 nm, 603 nm, while negative peaks are observed at 426 nm, 551 nm, 594 nm. Difference of difference absorbance (ΔΔAbs) were obtained after subtracting the negative absorbance at 426 nm from positive absorbance at 437 nm during each Fe(II) addition and is plotted as a function of Fe(II) concentration and shown in the inset. The difference of difference plot (ΔΔAbs vs. Fe(II) concentration) is analyzed by least square fits using the following equation[5]: $y = y_{\max} * ([(P + x + k_D) - \{(P + x + k_D)^2 - (4 * P * x)\}^{\frac{1}{2}}] / 2 * P)$, where $P$ = protein concentration, x = Fe(II) concentration, and $K_d$ = dissociation constant. From this analysis, a dissociation constant of 7.2 μM is extracted. Parameters from fit: Reduced Chi-Sqr = 9.45298E-6, Adj. R-Square = 0.9976, P = 7 ± 0 μM, $K_d$ =7.24339 ± 0.35058 μM, $y_{max}$ = 0.2454 ± 0.00328.

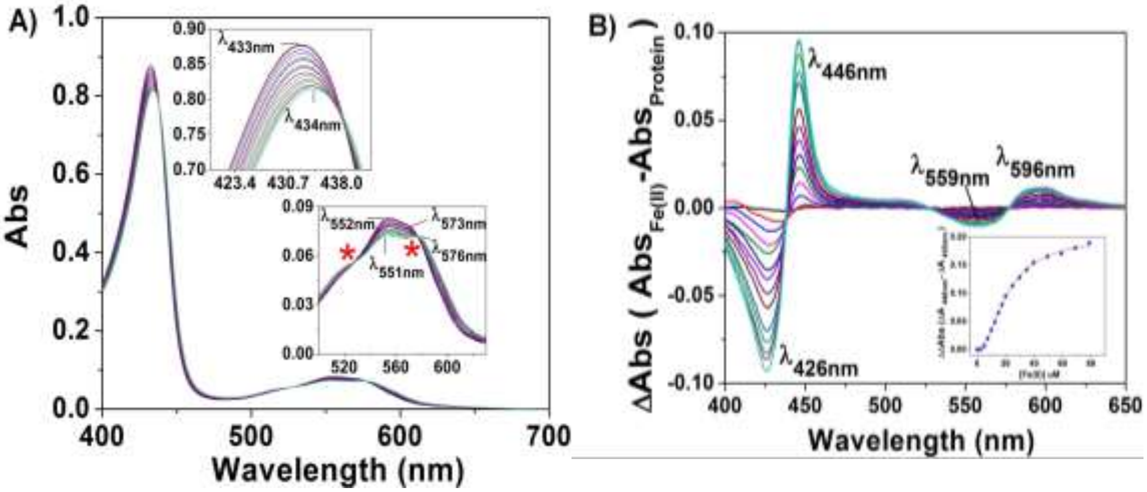

**Figure S4. A)** UV-vis spectra obtained during titration of aliquots of $FeCl_2$ to 7 μM deoxy $Fe_BMb1$ in 50 mM Bis-Tris pH 7.3. $Fe_BMb1$ was reduced in the glove bag with dithionite. Titration was performed outside the glove bag by adding aliquots of degassed $FeCl_2$ to the deoxy protein in a gas tight cuvette using a gas tight syringe. Spectral changes were monitored using a Cary 3E UV-vis spectrometer. Insets show blow-ups of the Soret and visible regions. Isosbestic points at 529 nm, and 578 nm are shown as red stars. **B)** Difference spectra (ΔAbs vs. λ) obtained after subtracting the metallated spectra from the spectrum without Fe(II). Positive peaks are observed at 446 nm, 596 nm, while negative peaks are observed at 426 nm, 559 nm. Difference of difference absorbance (ΔΔAbs) are obtained after subtracting the negative absorbance at 426 nm from positive absorbance at 446 nm during each Fe(II) addition and is plotted as a function of Fe(II) concentration and shown in the inset. Attempts to analyze the difference of difference plot (ΔΔAbs vs. Fe(II) concentration) using the equation shown in Figure S4 resulted in poor fits. Thus, this data was analyzed by least square fits using the Hill equation: $y = y_{\max} * x^n /(k_D{}^n + x^n)$, as the shape of the curve implies cooperative Fe(II) binding. x = Fe(II) concentration, $K_d$ = dissociation constant, n = number of cooperative sites. From this analysis, a dissociation constant of 21.5 μM is extracted. Parameters from fit are: Reduced Chi-Sqr = 6.85786E-6, Adj. R-Square = 0.998, $K_d$ = 21.5 ± 0.5 μM, $y_{max}$ = 0.19796 ± 0.00319, n = 2.002 ± 0.0069. The analysis implies there are two cooperative Fe(II) binding sites.

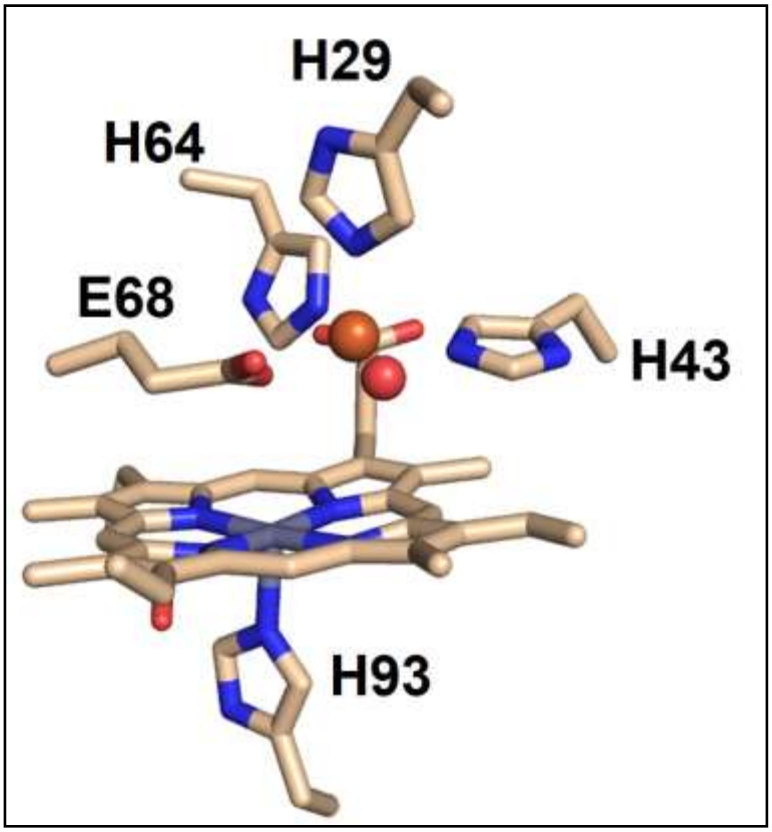

**Figure S5.** PyMol representation of the X-ray structure of Fe(II)-ZnPPFe$_B$Mb refined to 1.52 Å. Non-heme Fe atom is shown as orange sphere, and the water molecule as red sphere. The anomalous map generated from data collected below Fe K-edge at 7.0 keV and drawn at contour 7$\sigma$ does not show any anomalous electron density around the non-heme Fe atom as no anomalous map is visible, in contrast to the anomalous data collected above Fe K-edge (7.2 keV), and the resulting anomalous map drawn at 7$\sigma$ shown in Fig 3, where the clear presence of the anomalous electron density can be seen. Coordinates and structure factors have been deposited with the PDB code 4MXK,

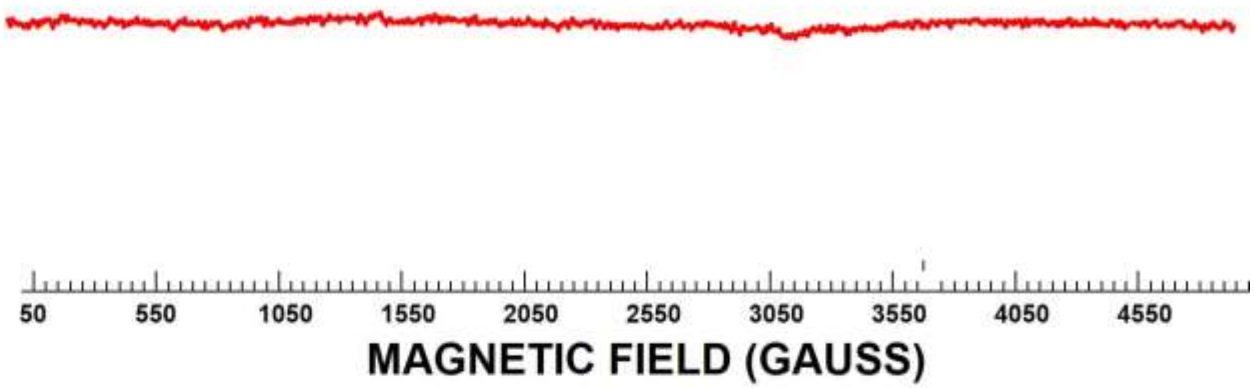

**Figure S6.** X-band EPR of a sample containing 600 μM Fe(II)-ZnPPFe$_B$Mb1 in 50 mM Bis-Tris pH 7.3. T=6K, microwave frequency=9.053 GHz, microwave power = 20 dB, mod amp = 4 G. The sample is EPR silent as expected for singlet spin systems.

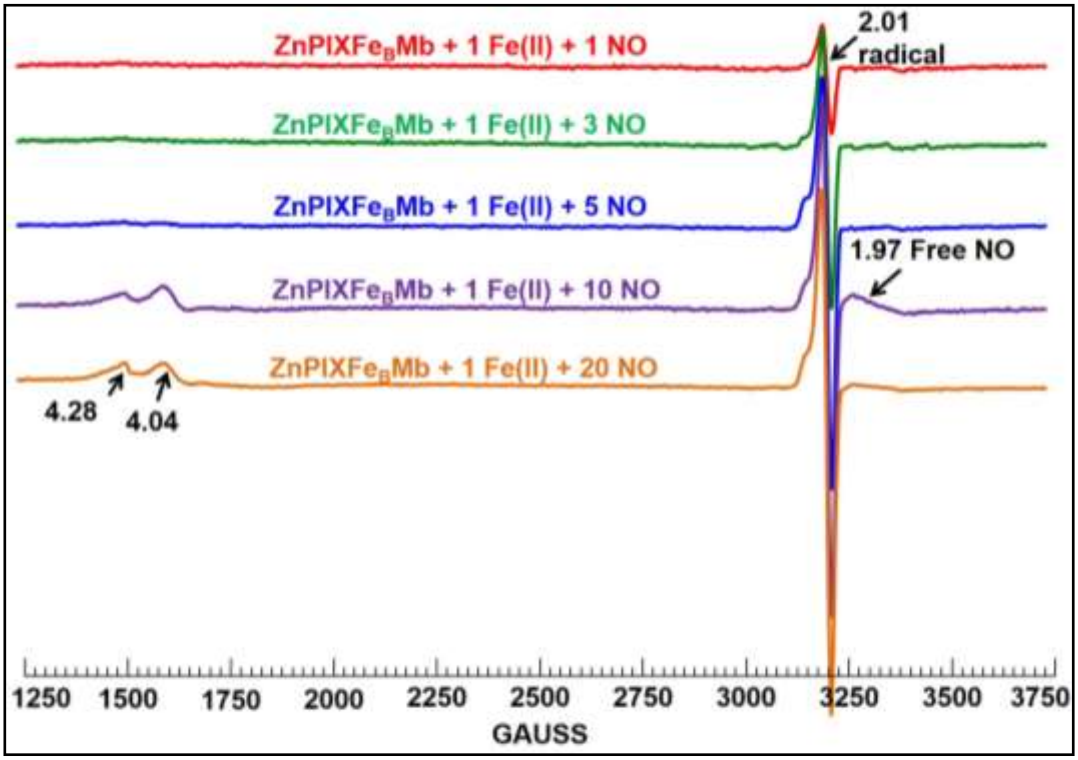

**Figure S7.** EPR spectra of samples containing 250 μL of 300 μM ZnPPFe$_B$Mb1 in 50 mM Bis-Tris pH 7.3, 0.9 eq. Fe(II), 0-20 eq. NO. 22% glycerol was added as glassing agent. Samples were prepared anaerobically in a glove bag, and flash frozen in liquid $N_2$ outside the glove bag immediate after taking out of the bag. These samples were not subjected to PD10 column after NO addition, and thus contain adventitiously bound iron at *g* ~ 4.28, and free NO at *g* ~ 1.97. Experimental parameters: T = 30K, microwave frequency = 9.053 GHz, microwave power = 0.5 mW, modulation amplitude = 4 G. From EPR simulations, the population of the radical-like peak at ~2.01 was obtained to be ~8%.

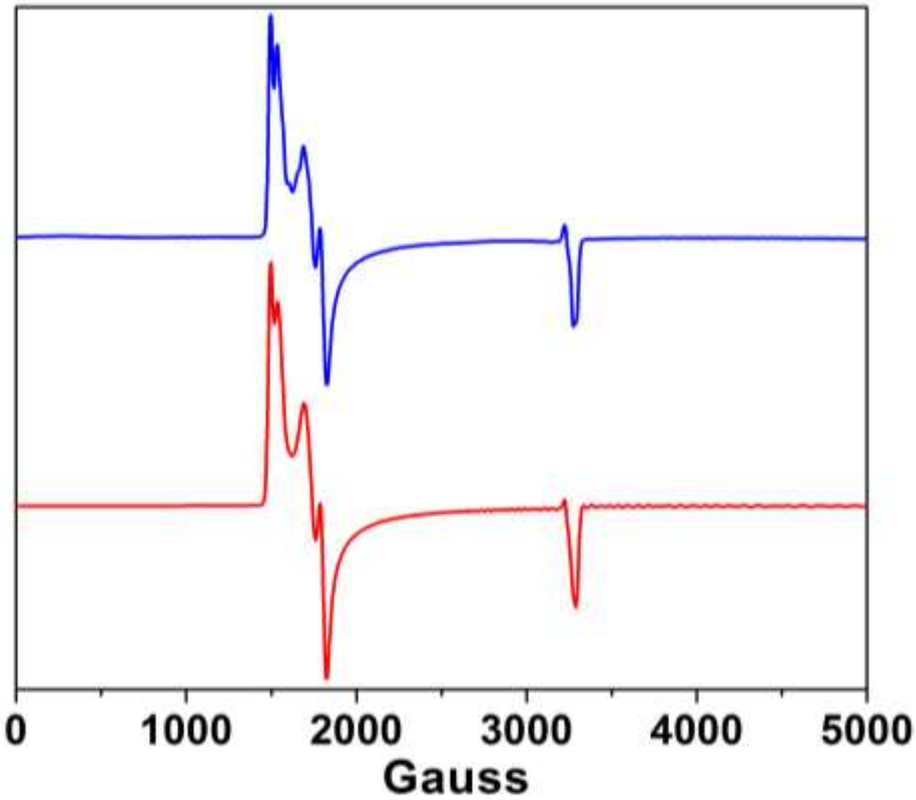

**Figure S8.** Full scale EPR spectrum (blue trace) of a sample containing 250 μL of 700 μM Fe(II)-ZnPPFe$_B$Mb1 in 50 mM Bis-Tris pH 7.3 in the presence of 20 equivalents of NO. Experimental parameters: T = 5K, microwave frequency = 9.053 GHz, microwave power = 20 dB, modulation amplitude = 4 G. Simulation of this spectrum is shown as red trace.

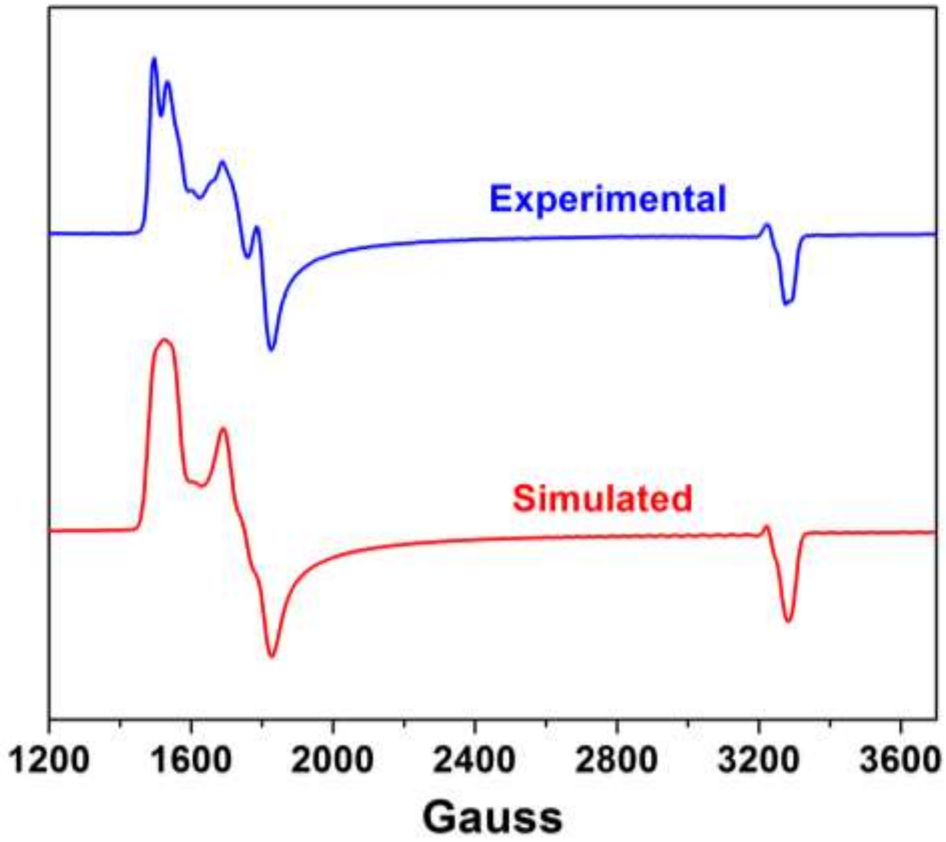

**Figure S9.** Simulation (red) of the data (blue) shown in Figure S8 taking into account the $^{14}$N hyperfine interaction. Clearly the simulated spectrum cannot reproduce the experimental data as the resolution of the peaks around *g*~4 are blurred and not resolved.

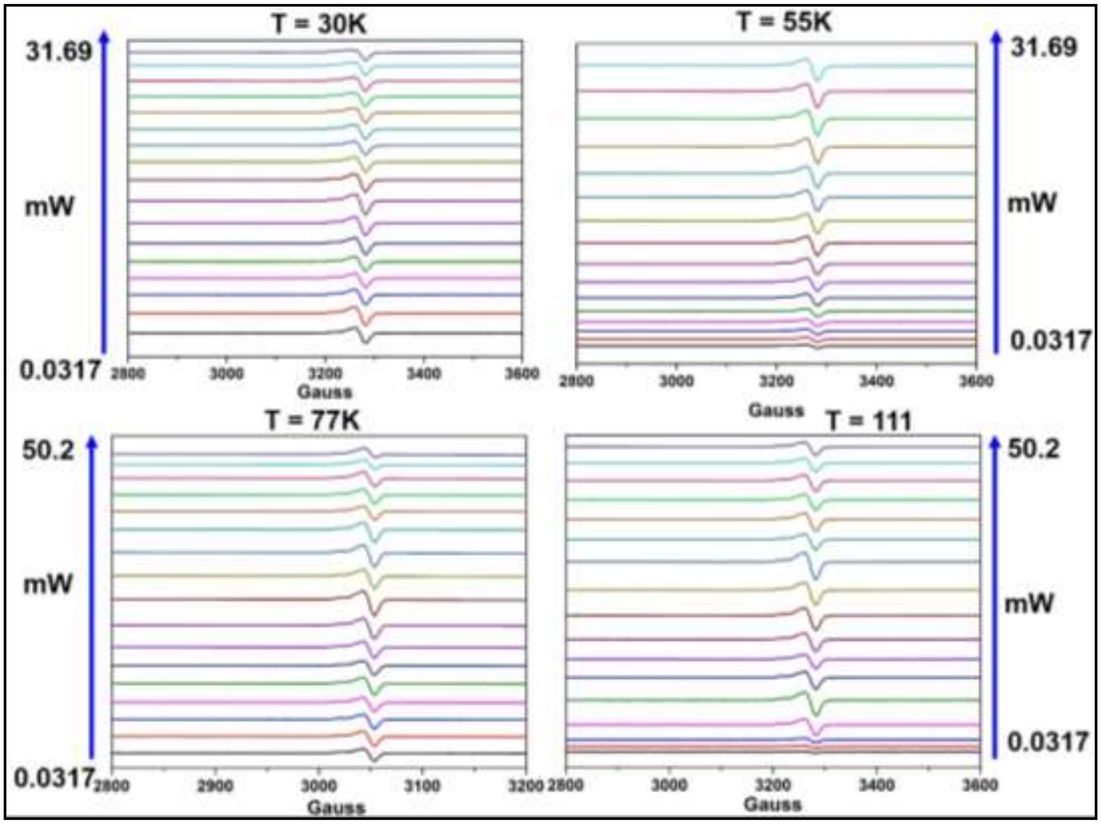

**Figure S10.** EPR spectra of a sample containing 500 μM Fe(II)-ZnPPFeBMb1 and 20 eq. NO in 50 mM Bis-Tris pH 7.3, recorded at 30K, 55K, 77K, and 111K under varying microwave power from 0.0317 mW (38 dB) to 31.69 (8 dB) or 50.2 mW (6 dB). Microwave frequency = 9.242 GHz, modulation amplitude = 4G.

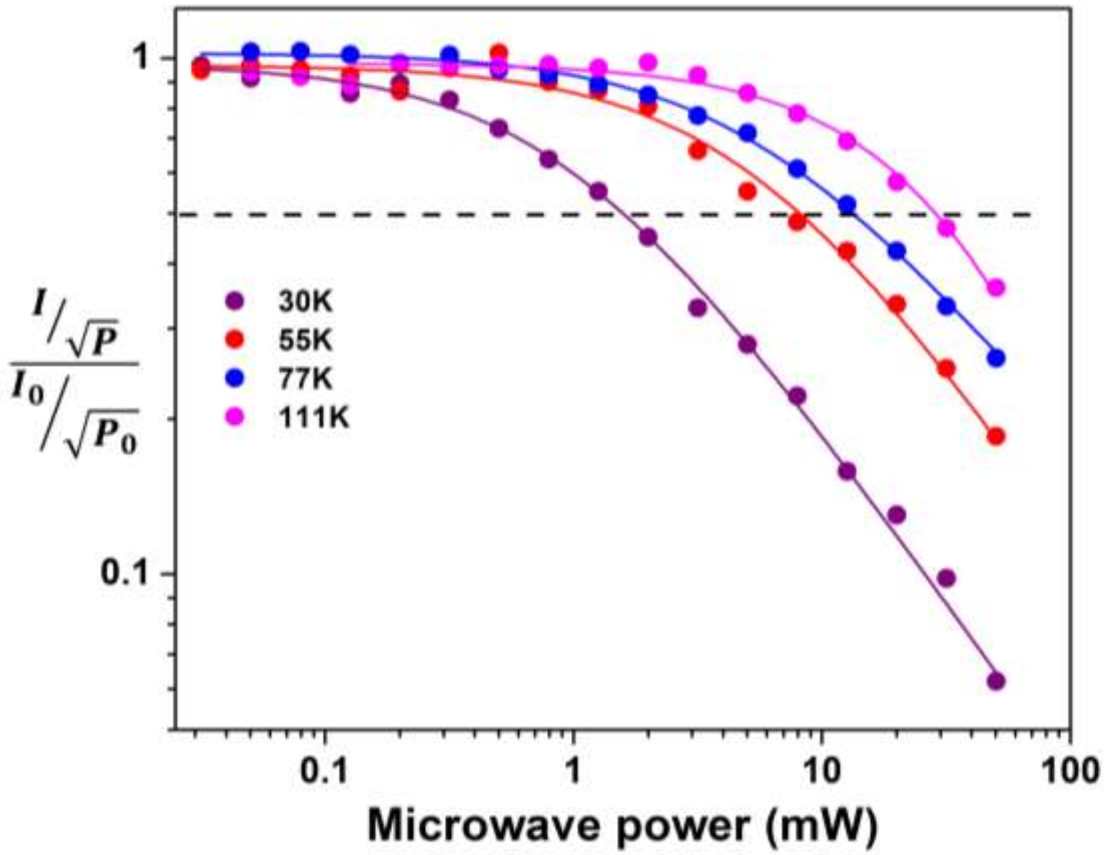

**Figure S11.** Plots of intensity/√P vs. microwave power (mW) of the sharpest peak at *g* ~ 2.01 for the temperature-dependent power saturation data shown in Figure S10. $I_0$ is the intensity at the lowest power $P_0$. The plots were analyzed by using the equation:[7a-d]

$$I/\sqrt{P} = \frac{K}{\left[1 + \left(2^{\left(\frac{2}{B}\right)} - 1\right) * \left(\frac{P}{P_{1/2}}\right)\right]^{\frac{b}{2}}}$$

where I = peak-to peak intensity, K = constant, P = microwave power in mW, b = measure of homogeneity of the line shape with a value varying between 1 and 3, $P_{1/2}$ is the microwave power at which the amplitude of the EPR signal is one-half of its unsaturated value. The results of this analysis are shown in Table S1. The $P_{1/2}$ values can also be read from the plot directly where the dotted horizontal line intersects the experimental curves. The $P_{1/2}$ values indicate that the radical is associated with the metal.

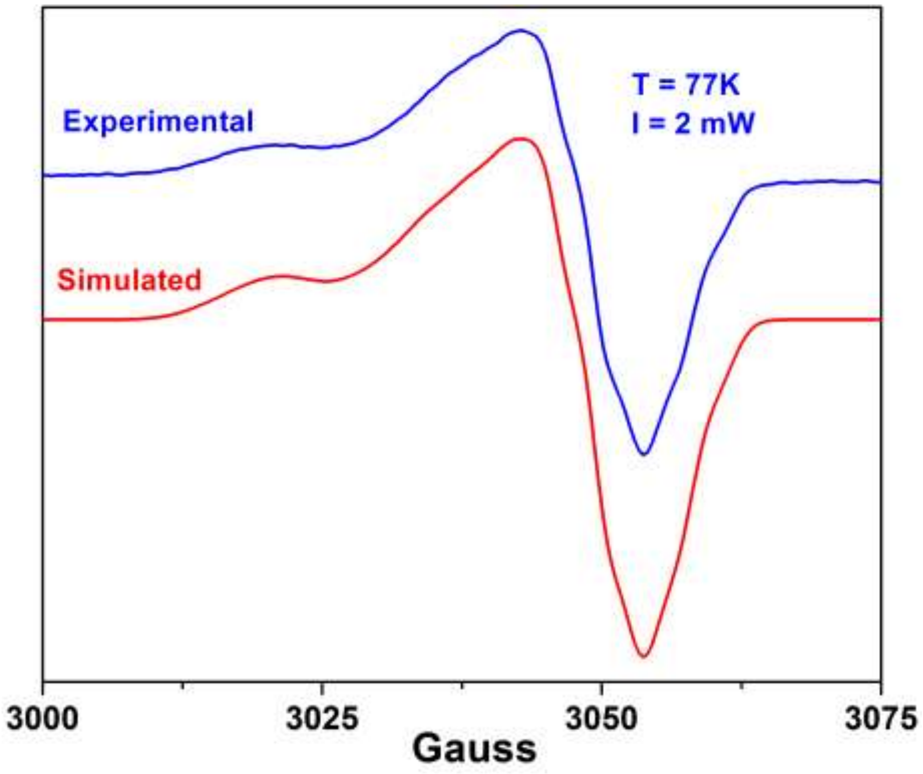

**Figure S12.** Experimental (blue) and simulated (red) EPR spectra of the peak at *g* ~ 2.01 for the data recorded at 77K with microwave power 2 mW as shown in Figure S10. Extracted parameters from simulation are shown in Table S2. Relative population of this radical-like peak is obtained to be ~5% from simulation. The low-field region of the spectrum corresponding to the S=3/2 signals is not shown.

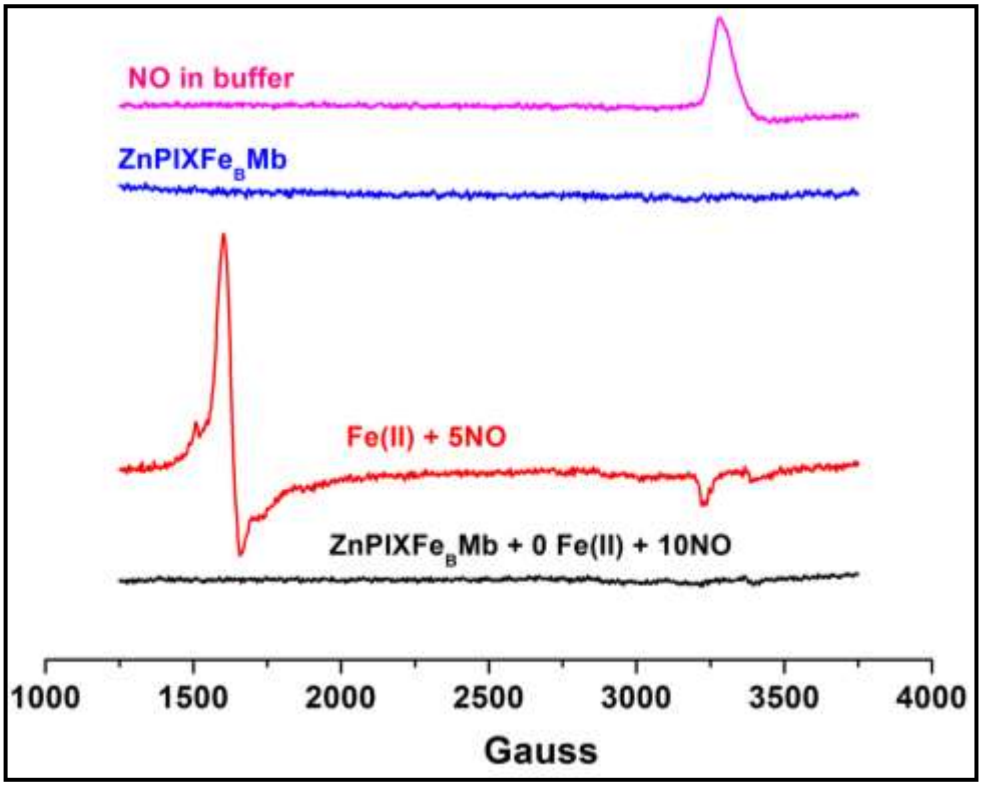

**Figure S13.** EPR spectra of samples containing 250 μL of 6 mM NO in 50 mM Bis-Tris pH 7.3 (magenta), 300 μM ZnPPFe$_B$Mb1 in 50 mM Bis-Tris pH 7.3 (blue), 300 μM $FeCl_2$ + 1.5 mM NO (red), and 300 μM ZnPPFe$_B$Mb1 in 50 mM Bis-Tris pH 7.3 + 3 mM NO (black). 22% glycerol was added as glassing agent. Samples were prepared anaerobically in a glove bag, and flash frozen in liquid $N_2$ outside the glove bag immediate after taking out of the bag. Experimental parameters: T = 30K, microwave frequency = 9.053 GHz, microwave power = 0.5 mW, modulation amplitude = 4 G. Traces shown in blue and black have no detectable EPR signal, and the signals for "free" NO and HS Ferric-NO are magenta and red, respectively. These control experiments show that the EPR features shown in Figure 5, Figures S7, S8, and S9 can be observed only when NO is present in Fe(II) incorporated in the non-heme site of ZnPPFe$_B$Mb1.

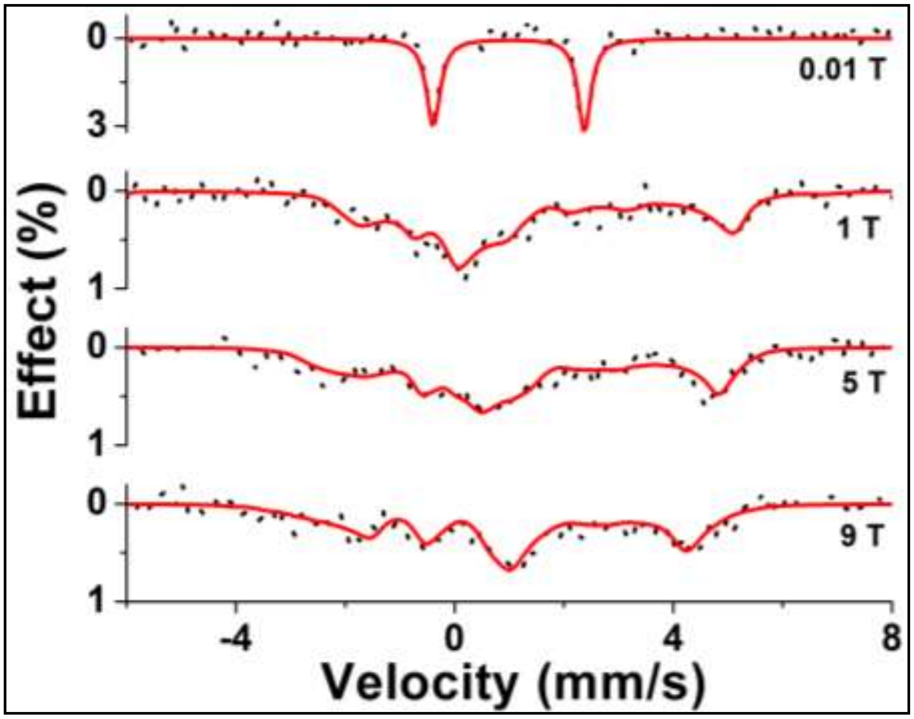

**Figure S14.** Field-dependent Mössbauer spectra of a sample containing 200 μL of ~3.5 mM $^{57}$Fe(II)-ZnPPFe$_B$Mb1 in 50 mM Bis-Tris pH 7.3. Experimental conditions: T=4.2K, H = 0.01 - 9 T. The simultaneous fitting of the spectra yield the following parameters, $\delta_{Fe}$ = 1.13 mm/s, $\Delta E_Q$ = 2.84 mm/s, E/D = 0.19, $\Gamma$ = 0.35 mm/s, implying that $^{57}$Fe(II) is bound in the non-heme site of ZnPPFe$_B$Mb1 as HS ferrous in a rhombic geometry. Fitted parameters are shown in Table S3. 0.01T data were fit with fast relaxation model, while the 1-9T data were fit using slow relaxation model.

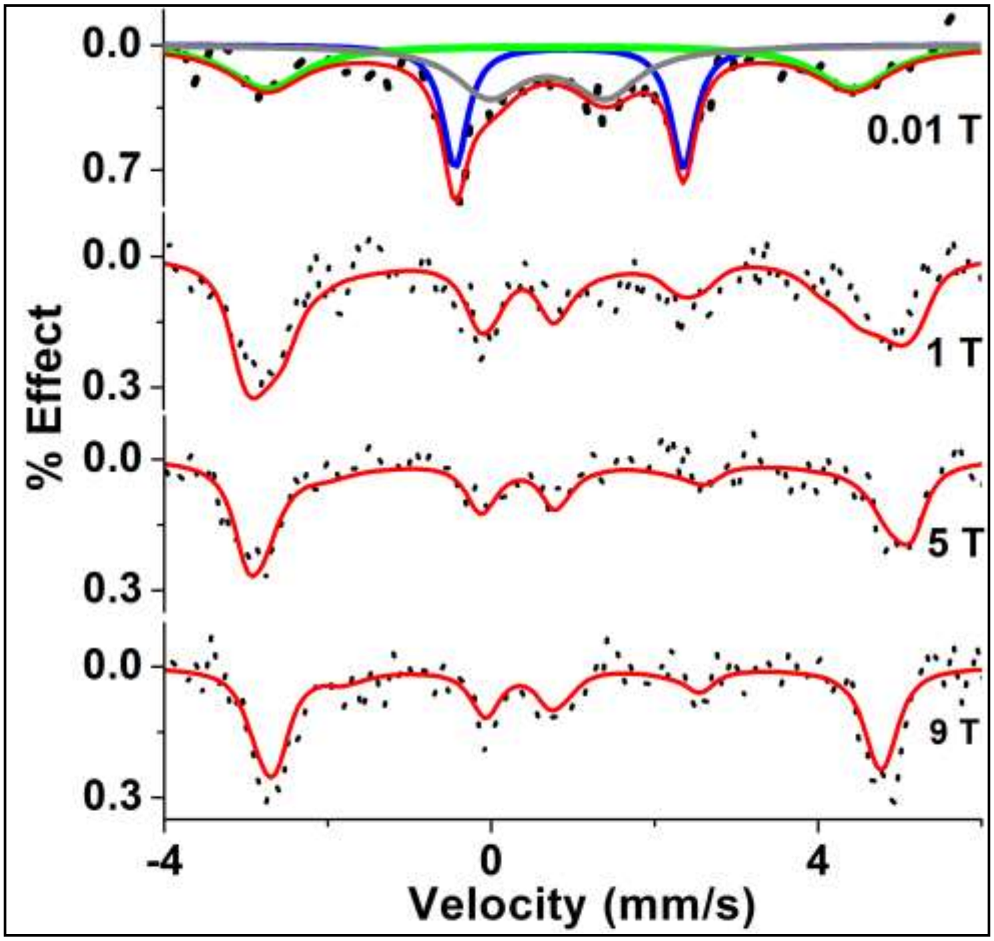

**Figure S15.** Field-dependent Mössbauer spectra of a sample containing 7 mM $^{57}$Fe(II)-ZnPPFe$_B$Mb1, and 20 equivalents of NO in 50 mM Bis-Tris pH 7.3, collected at 4.2K. Black dots: experimental data; red lines: sum of fit; blue line: ferrous S=2 starting material; gray line: S=3/2 {FeNO}$^7$ component in intermediate relaxation; green line: magnetically split S=3/2 {FeNO}$^7$ component. Only the splitting pattern of 65% S=3/2 {FeNO}$^7$ species is shown in high field. The S=3/2 species at all fields was simulated using a slow relaxation model. The S=2 species in low-field was simulated as Lorentzian.

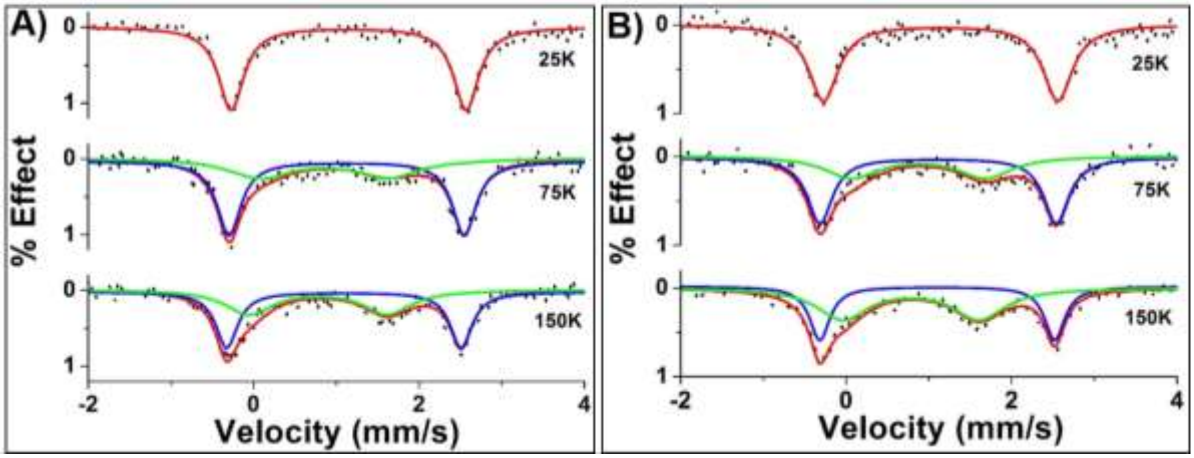

**Figure S16.** Mössbauer spectra of a sample containing 200 μL of ~6 mM $^{57}$Fe-ZnPPFe$_B$Mb1 and 1.0 eq. NO (A), and 5.0 eq. NO (B) in 50 mM Bis-Tris pH 7.3, collected at 25K, 75K, and 150K in low field (0.01T). The parameters of the S=2 Fe(II) starting material (blue lines) and the S=3/2 {FeNO}$^7$ species (green lines) extracted from the non-linear least square analyses of these spectra are shown in Table S4. Due to intermediate relaxation of the {FeNO}$^7$ complex leading to spectral broadening, this species cannot be detected at 25K. At high temperatures, 75K, and 150K, the {FeNO}$^7$ species is in the fast relaxation regime and can be detected and deconvoluted. Black dots: raw data, red lines: sum of fits, blue line: S=2 Fe(II), green line: S=3/2 {FeNO}$^7$ complex. The IS and QS values obtained from these data (Table S4) are close to the values obtained from the high field data measured at 4.2 K containing 20 eq. of NO. At higher temperatures all of the S=3/2 species is close to the fast relaxation limit for which the magnetic hyperfine splitting collapses to a single doublet (green lines), unlike at low temperature where a magnetically split component is also observed (Figure 6: short dotted gray line, Figure S15: green line). The position of the S=3/2 doublet shown in green is similar to the S=3/2 species present in intermediate relaxation at 4.2K with 20 eq. NO (Figure 6: gray dashed line, Figure S15: gray solid line), indicating that the same S=3/2 species is formed irrespective of temperature and NO equivalents. For all the simulations spectra in Figure S16 were fit with Lorentzian lines.

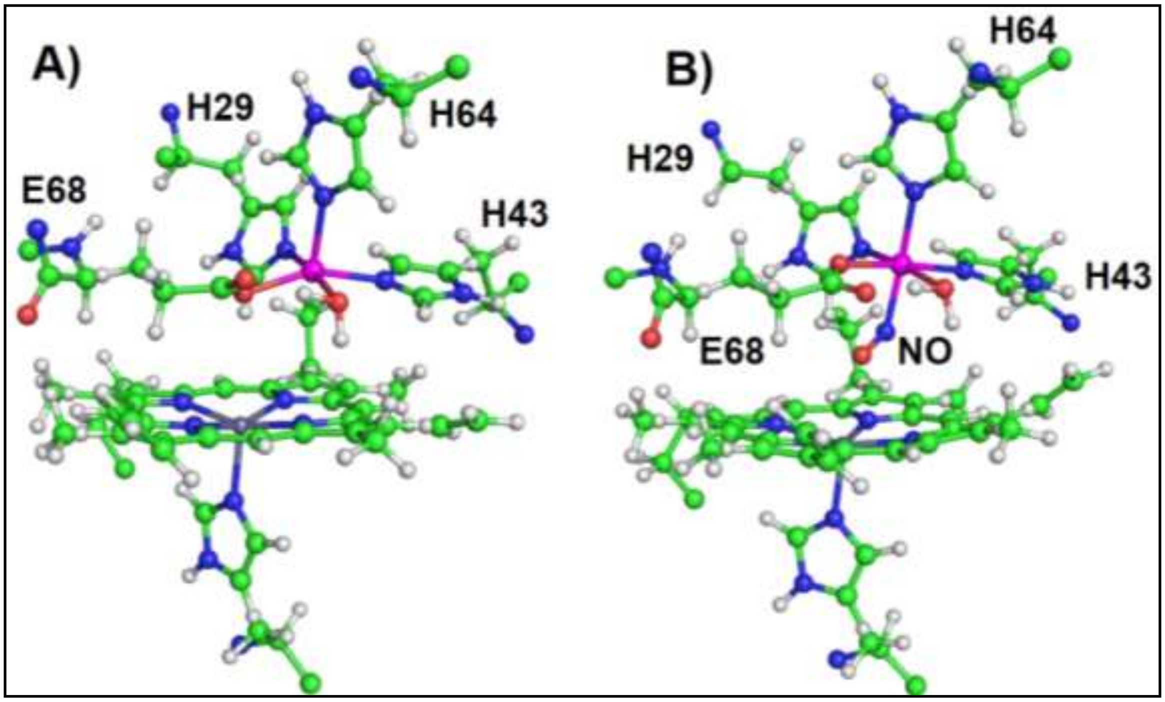

**Figure S17.** QM/MM optimized structures of Fe(II)-ZnPPFeBMb1 without (A), and with NO (B). Color scheme: C – green, Fe – magenta, N – blue, O – red, H – grey.

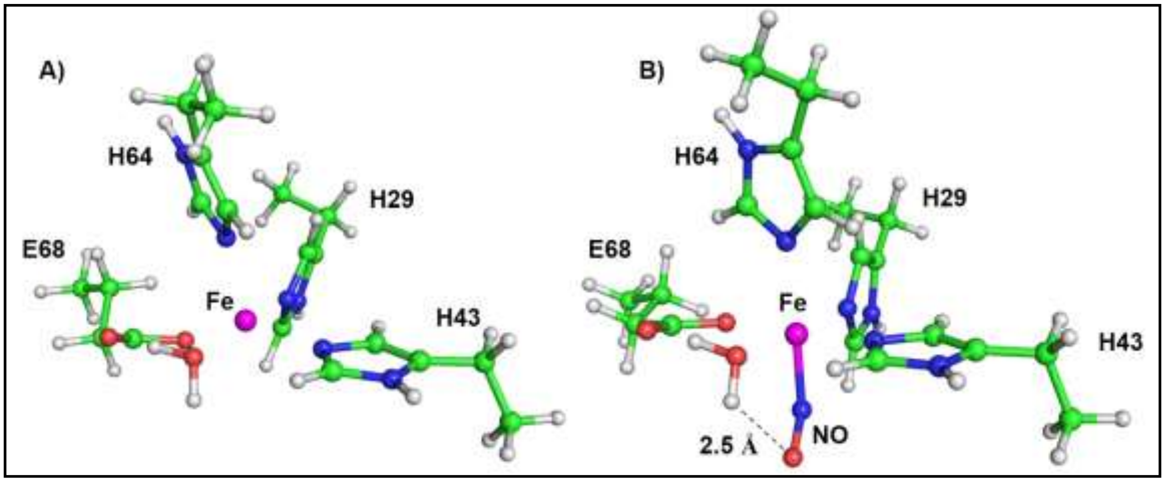

**Figure S18.** Optimized active site structures of NO-free (A) and NO-bound Fe(II)-ZnPPFe$_B$Mb1 (B). Color scheme: C – green, Fe – magenta, N – blue, O – red, H – grey.

## References:

[1] N. Yeung, Y.-W. Lin, Y.-G. Gao, X. Zhao, B. S. Russell, L. Lei, K. D. Miner, H. Robinson, Y. Lu, *Nature* **2009**, *462*, 1079-1082.
[2] F. W. J. Teale, *Biochim. Biophys. Acta* **1959**, *35*, 543.
[3] M. Morrison, S. Horie, *Anal. Biochem.* **1965**, *12*, 77-82.
[4] J. J. Leonard, T. Yonetani, J. B. Callis, *Biochemistry* **1974**, *13*, 1460-1464.
[5] A. Bidwai, M. Witt, M. Foshay, L. B. Vtello, J. D. Satterlee, J. E. Erman, *Biochemistry* **2003**, *42*, 10764-10771.
[6] J. T. Weisser, M. J. Nilges, M. J. Sever, J. J. Wilker, *Inorg. Chem.* **2006**, *45*, 7736-7747.
[7] a) S. S. Eaton, G. R. Eaton, *Coord. Chem. Rev.* **1978**, *26*, 207-262; b) M. Sahlin, L. Petersson, A. Graeslund, A. Ehrenberg, B. M. Sjoeberg, L. Thelander, *Biochemistry* **1987**, *26*, 5541-5548; c) T. Sarna, J. S. Hyde, H. M. Swartz, *Science* **1976**, *192*, 1132-1134; d) Y. G. Yu, T. E. Thorgeirsson, Y.-K. Shin, *Biochemistry* **1994**, *33*, 14221-14226; e) A. B. Tomter, G. Zoppellaro, C. B. Bell III, A.-L. Barra, N. H. Andersen, E. I. Solomon, K. K. Andersson, *PloS one* **2012**, *7*, e33436.
[8] V. Schünemann, C. Jung, A. X. Trautwein, D. Mandon, R. Weiss, *FEBS Lett.* **2000**, *479*, 149-154.
[9] a) T. C. Harrop, M. M. Olmstead, P. K. Mascharak, *Inorg. Chem.* **2005**, *44*, 6918-6920; b) M. Li, D. Bonnet, E. Bill, F. Neese, T. Weyhermüller, N. Blum, D. Sellmann, K. Wieghardt, *Inorg. Chem.* **2002**, *41*, 3444-3456; c) R. G. Serres, C. A. Grapperhaus, E. Bothe, E. Bill, T. Weyhermüller, F. Neese, K. Wieghardt, *J. Am. Chem. Soc.* **2004**, *126*, 5138-5153; d) A. C. McQuilken, Y. Ha, K. D. Sutherlin, M. A. Siegler, K. O. Hodgson, B. Hedman, E. I. Solomon, G. N. Jameson, D. P. Goldberg, *J. Am. Chem. Soc.* **2013**, *135*, 14024-14027.
[10] Z. Otwinowski, W. Minor, in *Methods in Enzymology: Macromolecular Crystallography, part A, Vol. 276* (Eds.: C. W. J. Carter, R. M. Sweet), Academic Press, New York, **1997**, pp. 307-326.
[11] A. Vagin, A. Teplyakov, *J. Appl. Crystallogr.* **1997**, *30*, 1022-1025.
[12] M. D. Winn, C. C. Ballard, K. D. Cowtan, E. J. Dodson, P. Emsley, P. R. Evans, R. M. Keegan, E. B. Krissinel, A. G. W. Leslie, A. McCoy, S. J. McNicholas, G. N. Murshudov, N. S. Pannu, E. A. Potterton, H. R. Powell, R. J. Read, A. Vagin, K. S. Wilson, *Acta Crystallogr. Sect. D-* **2011**, *67*, 235-242.
[13] G. N. Murshudov, P. Skubak, A. A. Lebedev, N. S. Pannu, R. A. Steiner, R. A. Nicholls, M. D. Winn, F. Long, A. A. Vagin, *Acta Crystallogr. Sect. D-* **2011**, *67*, 355-367.
[14] P. Emsley, K. Cowtan, *Acta Cryst. D* **2004**, *60*, 2126-2132.
[15] P. D. Adams, P. V. Afonine, G. Bunkoczi, V. B. Chen, I. W. Davis, N. Echols, J. J. Headd, L.-W. Hung, G. J. Kapral, R. W. Grosse-Kunstleve, A. J. McCoy, N. W. Moriarty, R. Oeffner, R. J. Read, D. C. Richardson, J. S. Richardson, T. C. Terwilliger, P. H. Zwart, *Acta Crystallogr. Sect. D-* **2010**, *66*, 213-221.
[16] W. L. DeLano, *The PyMOL Molecular Graphics System, DeLano Scientific, Palo Alto, California, USA 2005, http://www.pymol.org.*
[17] a) Desmond Molecular Dynamics System, v. 3.1, D. E. Shaw Research, New York, **2012**; b) Maestro-Desmond Interoperability Tools, v. 3.1, Schrödinger, New York, **2012**.
[18] Y. Duan, C. Wu, S. Chowdhury, M. C. Lee, G. Xiong, W. Zhang, R. Yang, P. Cieplak, R. Luo, T. Lee, *J. Comput. Chem.* **2003**, *24*, 1999-2012.
[19] L. Zhang, D. A. Silva, Y. Yan, X. Huang, *J. Comput. Chem.* **2012**, *33*, 1969-1980.
[20] a) A. D. Becke, *Phys. Rev. A.* **1988**, *38*, 3098-3100; b) A. D. Becke, *J. Chem. Phys.* **1993**, *98*, 5648-5652; c) C. T. Lee, W. T. Yang, R. G. Parr, *Phys. Rev. B* **1988**, *37*, 785-789; d) P. J. Stephens, F. J. Devlin, C. F. Chabolowski, M. J. Frisch, *J. Phys. Chem.* **1994**, *98*, 11623-11627; e) S. H. Vosko, L. Wilk, M. Nusair, *Can. J. Phys.* **1980**, *58*, 1200-1211.

[21] a) P. J. Hay, W. R. Wadt, *J. Chem. Phys.*, *82*, 270-283; b) W. R. Wadt, P. J. Hay, *J. Chem. Phys.* **1985**, *82*, 284-298.
[22] QSite, v. 5.0, Schrodinger, LLC, New York, **2008**.
[23] a) J. P. Perdew, *Phys. Rev. B* **1986**, *33*, 882; b) J. P. Perdew, *Phys. Rev. B (Erratum)* **1986**, *34*, 7406.
[24] a) W. L. Jorgensen, D. S. Maxwell, J. Tirado-Rives, *J. Am. Chem. Soc.* **1996**, *118*, 11225-11236; b) W. L. Jorgensen, J. Tirado-Rives, *J. Am. Chem. Soc.* **1988**, *110*, 1657-1666.
[25] W.-G. Han, T. Liu, T. Lovell, L. Noodleman, *J. Comput. Chem.* **2006**, *27*, 1292-1306.
[26] Y. Zhang, E. Oldfield, *J. Am. Chem. Soc.* **2004**, *126*, 9494-9495.
[27] L. T. Haahr, K. P. Jensen, J. Boesen, H. E. M. Christensen, *J. Inorg. Biochem.* **2010**, *104*, 136-145.
[28] J. Katigbak, Y. Zhang, *J. Phys. Chem. Lett.* **2012**, *3*, 3503-3508.
[29] a) Y. Zhang, W. Gossman, E. Oldfield, *J. Am. Chem. Soc.* **2003**, *125*, 16387-16396; b) Y. Zhang, E. Oldfield, *J. Am. Chem. Soc.* **2004**, *126*, 4470-4471; c) R. Fu, R. Gupta, J. Geng, K. Dornevil, S. Wang, Y. Zhang, M. P. Hendrich, A. Liu, *J. Biol. Chem.* **2011**, *286*, 26541-26554; d) Y. Ling, V. L. Davidson, Y. Zhang, *J. Phys. Chem.Lett.* **2010**, *1*, 2936-2939.
[30] Y. Zhang, E. Oldfield, *Journal of Physical Chemistry A* **2003**, *107*, 4147-4150.
[31] Y. Zhang, J. H. Mao, N. Godbout, E. Oldfield, *J. Am. Chem. Soc.* **2002**, *124*, 13921-13930.
[32] Y. Zhang, J. H. Mao, E. Oldfield, *J. Am. Chem. Soc.* **2002**, *124*, 7829-7839.
[33] A. D. Becke, *J. Chem. Phys.* **1993**, *98*, 5648-5652.
[34] A. J. Wachters, *J. Chem. Phys.* **1970**, *52*, 1033-1036.
[35] a) Y. Zhang, E. Oldfield, *J.Phys. Chem. B.* **2003**, *107*, 7180-7188; b) Y. Ling, Y. Zhang, *J. Am. Chem. Soc.* **2009**, *131*, 6386-6388; c) Y. Ling, Y. Zhang, in *Annual Reports in Computational Chemistry, Vol. 6* (Ed.: R. A. Wheeler), Elsevier, New York, **2010**, pp. 65-77.
[36] P. Dufek, P. Blaha, K. Schwarz, *Phys. Rev. Lett.* **1995**, *75*, 3545-3548.
[37] Frisch, M. J.; Trucks, G. W.; Schlegel, H. B.; Scuseria, G. E.; Robb, M. A.; Cheeseman, J. R.; Scalmani, G.; Barone, V.; Mennucci, B.; Petersson, G. A.; Nakatsuji, H.; Caricato, M.; Li, X.; Hratchian, H. P.; Izmaylov, A. F.; Bloino, J.; Zheng, G.; Sonnenberg, J. L.; Hada, M.; Ehara, M.; Toyota, K.; Fukuda, R.; Hasegawa, J.; Ishida, M.; Nakajima, T.; Honda, Y.; Kitao, O.; Nakai, H.; Vreven, T.; Montgomery, Jr., J. A.; J. Peralta, E.; Ogliaro, F.; Bearpark, M.; Heyd, J. J.; Brothers, E.; Kudin, K. N.; Staroverov, V. N.; Keith, T.; Kobayashi, R.; Normand,J.; Raghavachari, K.; Rendell, A.; Burant, J. C.; Iyengar, S. S.; Tomasi, J.; Cossi, M.; Rega, N.; Millam, J. M.; Klene, M.; Knox, J. E.; Cross, J. B.; Bakken, V.; Adamo, C.; Jaramillo, J.; Gomperts, R.; Stratmann, R. E.; Yazyev, O.; Austin, A. J.; Cammi, R.; Pomelli, C.; Ochterski, J. W.; Martin, R. L.; Morokuma, K.; Zakrzewski,V. G.; Voth, G. A.; Salvador, P.; Dannenberg, J. J.; Dapprich, S.; Daniels, A. D.; Farkas, O.; Foresman, J. B.; Ortiz, J. V.; Cioslowski, J.; Fox, D. J.; Gaussian 09, Revision B.01 ed., Gaussian, Inc., Wallingford CT, **2010**.
[38] F. Biegler-König, AIM2000, Version 2.0 ed., University of Applied Science, Bielefeld, Germany, **2002**.
[39] L. Yang, Y. Ling, Y. Zhang, *J. Am. Chem. Soc.* **2011**, *133*, 13814-13817.
[40] a) A. D. Becke, *Phys. Rev. A.* **1988**, *38*, 3098-3100; b) J. P. Perdew, K. Burke, Y. Wang, *Phys. Rev. B.* **1996**, *54*, 16533-16539.
[41] a) J. Li, K. Wang, T. I. Smirnova, R. L. Khade, Y. Zhang, E. Oldfield, *Angew. Chem. Int. Ed.* **2013**, *52*, 6522-6525; b) Y.-L. Liu, F. Guerra, K. Wang, W. Wang, J. Li, C. Huang, W. Zhu, K. Houlihan, Z. Li, Y. Zhang, S. K. Nair, E. Oldfield, *Proc. Natl. Acad. Sci. U. S. A.* **2012**, *109*, 8558-8563; c) K. Wang, W. Wang, J. H. No, Y. Zhang, Y. Zhang, E. Oldfield, *J. Am. Chem. Soc.* **2010**, *132*, 6719-6727.